Measurement and prediction of momentum transport in spherical tokamaks

W. Guttenfelder[1], A.R. Field[2], I. Lupelli[2], J.-K. Park[1], T. Tala[3], J. Candy[4], S. Ethier[1], S.M. Kaye[1], Y. Ren[1], W.M. Solomon[4], W.X. Wang[1]

[1] Princeton Plasma Physics Laboratory, Princeton NJ 08543, USA
[2] CCFE, Culham Centre for Fusion Energy, Abingdon, Oxfordshire OX14 3DB, UK
[3] VTT, P.O. Box 1000, FIN-02044 VTT, Espoo, Finland
[4] General Atomics, San Diego, CA 92186, USA
E-mail contact of main author: wgutten@pppl.gov

Abstract. The inward momentum convection or "pinch" observed in many tokamaks can be explained by the Coriolis drift mechanism, with relatively good quantitative agreement found with gyrokinetic predictions of the ion temperature gradient (ITG) instability. Here we attempt to validate this model over a broader range of beta and aspect ratio by extending into the spherical tokamak (ST) plasma regime using data from NSTX and MAST. Previous perturbative measurements in NSTX H-modes have indicated the existence of an inward momentum pinch with a magnitude similar to that observed in conventional aspect ratio tokamaks. However, linear gyrokinetic simulations run for these cases predict the microtearing mode, which only transports electron energy, is the dominant micro-instability in the region of interest due to the relatively large plasma beta (β_N=3.5-4.6). Although weaker, there is also evidence of a variety of unstable electrostatic and electromagnetic ballooning modes including ITG, compressional ballooning modes (CBM), and kinetic ballooning modes (KBM). Quasi-linear calculations for all of these ballooning modes, assuming they contribute substantially to the momentum transport, predict a pinch that is small or directed outward, in contradiction to the experimental results. Additional scans show that the weak pinch is a consequence of how both electromagnetic effects (at relatively large beta) and low aspect ratio influence symmetry-breaking of the instabilities. To minimize electromagnetic effects, similar experiments were performed in MAST L-mode plasmas at lower beta (β_N=2) using the time-dependent rotation response after the removal of a short n=3 applied magnetic field perturbation. The inferred inward pinch is similar in magnitude to conventional tokamaks and the NSTX H-modes. However, if experimental uncertainties due to non-stationary conditions are considered, a weak or outward pinch can be inferred. Linear gyrokinetic simulations indicate that for the low beta L-modes, the predicted momentum pinch is relatively small. While this falls within the experimentally inferred range, the uncertainties are practically too large to quantitatively validate the predictions. Future experiments in NSTX-U are planned to further investigate momentum transport in the lower beta ST L-mode plasmas for the use of theory validation.

1. Introduction

Strong toroidal rotation can improve both macroscopic stability and confinement in tokamak plasmas. In addition to torque sources and sinks, it is important to understand the transport mechanisms that determine the rotation profile in order to develop predictions for future devices such as ITER or a Fusion Nuclear Science Facility (FNSF). In addition to outward diffusion, there can be an inward momentum convection or "pinch" that has been observed in many tokamaks [1], as well as residual stress (or intrinsic torque) contributions [2,3]. In many cases the pinch can be explained by the Coriolis drift mechanism [4], with relatively good quantitative agreement found between experiment and theory predictions based on local, quasi-linear gyrokinetic calculations of the ion temperature gradient (ITG) instability (e.g. [5]). Here we attempt to validate this model over a broader range of beta and aspect ratio by extending into the spherical tokamak (ST) plasma regime using data from NSTX and MAST.

2. NSTX experiments and quasilinear gyrokinetic predictions

Previous perturbative measurements in NSTX H-modes have indicated the existence of an inward momentum pinch with a magnitude similar to that observed in conventional aspect ratio tokamaks [6].

Assuming a momentum flux of the form $\Pi = n_i m_i \langle R^2 \rangle (-\chi_\varphi \nabla\Omega + V_\varphi \Omega + \Pi_{RS})$, and neglecting any possible residual stress contributions (Π_{RS}=0), normalized pinch numbers of RV_φ/χ_φ=(-1)-(-7) (directed inward) were inferred.

Local, linear gyrokinetic simulations were run directly for these cases [7] using the GYRO code [8] to predict the magnitude of the Coriolis pinch. In all but one of the seven discharges investigated a broad spectrum ($k_\theta\rho_s$<1) of microtearing modes (MTM) is found to dominate with features similar to those predicted in many NSTX H-mode discharges [9]: electromagnetic instability with tearing-parity eigenfunctions (not shown), real frequencies that are proportional to the electron diamagnetic drift frequency, and the only substantial transport is in the electron thermal transport channel. Additional scans show the MTM to be driven unstable by electron temperature gradient at finite beta, due to the relatively large plasma beta of these discharges (β_T=12-16%, β_N=3.5-4.6).

While microtearing turbulence provides negligible momentum transport (compared to electron thermal transport), in these discharges there is also evidence of a variety of weaker yet unstable ballooning modes at lower wavenumbers ($k_\theta\rho_s$<0.3). Numerous parameter scans have been run to determine the nature of these modes, which includes ion temperature gradient (ITG) instability, compressional ballooning modes (CBM, which depend explicitly on the presence of compressional magnetic perturbations at high beta, e.g. [9,10]), and kinetic ballooning modes (KBM). The quasi-linear ratio of momentum to heat flux (Π/Q) from the linear GYRO simulations was used to predict the momentum pinch from these sub-dominant ballooning modes, assuming they contribute substantially to the momentum transport. In all cases investigated the predicted pinch number is small or directed outward ($RV_\varphi/\chi_\varphi \geq 0$) for all of the ballooning modes (ITG, KBM, CBM) in contradiction to the experimental results. Fig. 1 summarizes the range of measured and predicted pinch parameter for three NSTX H-modes in the region of interest (ρ≈0.5-0.7).

It has been noted previously that at increasing beta, the predicted inward Coriolis pinch is weakened for ITG turbulence due to electromagnetic effects, and can even reverse directions for the KBM [11]. In particular, the transport of momentum requires a breaking of symmetry in the unstable mode structure, and the electromagnetic effects at increasing beta tend to constrain this asymmetry thereby minimizing the pinch. Additional scans of the NSTX H-modes show that the predicted weak pinch is similarly a consequence of how electromagnetic effects at relatively large beta minimize the symmetry-breaking of the instabilities [7].

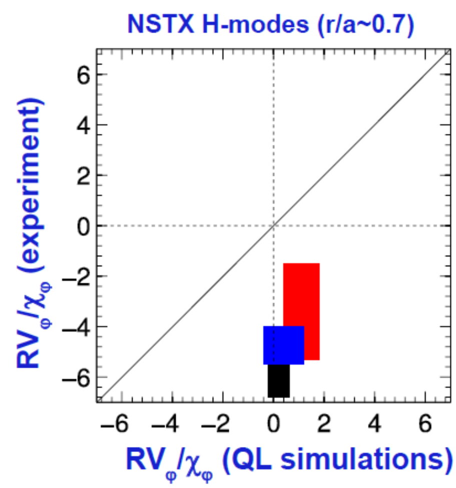

Fig. 1. Comparison of experimentally measured vs. predicted momentum pinch parameter, RV_φ/χ_φ for three NSTX H-mode discharges: (black) 134751, (red) 134778, (blue) 134779. (From Ref. [7])

To determine whether an inward momentum pinch is predicted in the ST for lower beta discharges, more consistent with theory for conventional aspect ratio, additional simulations were run for an NSTX L-mode discharge [12]. This discharge is at lower beta (β_T=7%, β_N=2.8) and linear gyrokinetic analysis predicts the outer half region of the plasma (ρ>0.5) is unstable to traditional electrostatic ITG-TEM turbulence. The calculated pinch number over a broad range of unstable wavenumbers is inward directed, RV_φ/χ_φ=(-1)-(-2), in contrast to the H-mode predictions. This inward pinch is more consistent with that observed and predicted in conventional tokamaks, although limited to relatively small magnitude.

Additional scans have been run to identify if parameters exist where a larger inward pinch would be predicted for the ITG-TEM modes at low aspect ratio. Scans over safety factor, magnetic shear, electron or ion temperature gradient, and collision frequency all show very weak dependencies. From theoretical analysis [4] as well multiple experimental observations [5], the influence of the local density gradient (R/L_n) has been predicted to be significant, with a proportionality $RV_\varphi/\chi_\varphi \sim -C_{\nabla n}\cdot R/L_n$ ranging between $C_{\nabla n}$=(0.4-1.2). Fig. 2a shows there is very little sensitivity of the predicted pinch to density gradient for the experimental case. However, if the density scan is repeated in the purely electrostatic limit ($\beta\rightarrow 0$), a stronger inward pinch is predicted at increased density gradient, with a proportionality that is similar to conventional aspect ratio tokamaks, $C_{\nabla n}\approx 0.5$, for $R/L_n>3$.

As there is a very large fraction of trapped particles $\sim(r/R)^{1/2}$ in these low aspect ratio discharges, it is of interest to investigate how the predicted pinch varies with minor radius or aspect ratio. This is especially relevant as trapped electrons can substantially influence the mode symmetry which influences the momentum pinch [13]. Two different scans were run using a local equilibrium expansion [14] that keep all other shaping and equilibrium parameters constant (as opposed to recalculating self-consistent global equilibria, e.g. as done in Ref. [15]). In the first scan, only the minor radius of the flux surface is varied (r/a), which has the largest effect of changing the strength of the $|B(\theta)|$ ripple and corresponding particle trapping, with a weaker variation in ∇B/curvature drifts and local magnetic shear. In the second scan, the aspect ratio was varied (a/R) while keeping the normalized flux surface (r/a) unchanged. While this approach similarly varies $|B(\theta)|$ and particle trapping, it also causes a larger variation to the ∇B/curvature drifts and local magnetic shear which can strongly influence stability (and is presumably more consistent with transitioning from low aspect ratio to high aspect ratio global equilibria). In either case, the growth rates of the ITG/TEM instability are weakened as particle trapping is reduced, indicating the importance of the trapped electrons to mode growth. Fig. 2b also shows that the corresponding pinch parameter exhibits a non-monotonic dependence on $(r/R)^{1/2}$. Increasing from the lowest particle trapping (small r/a, or large R/a) enhances the influence of the trapped electrons, which minimizes the so-called "compensation" effect [13], and initially allows for finite pinch. However, as the particle trapping increases further, the influence of the trapped electrons strongly symmetrizes the mode and ultimately weakens the pinch.

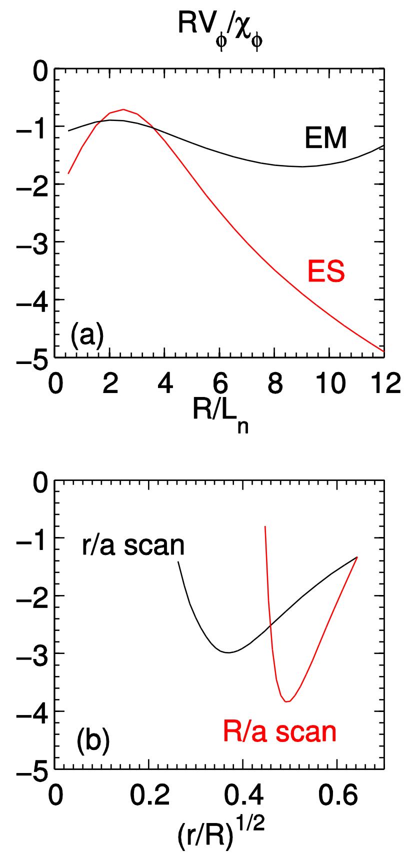

Fig. 2. Pinch parameter calculated for NSTX L-mode 141716 vs. (a) R/L_n and (b) $(r/R)^{1/2}$ ~ trapped particle fraction. (From Ref. [7].)

3. MAST L-mode experiment

The simulations performed for the NSTX L-mode case above suggest that a stronger momentum pinch may be expected at low aspect ratio in the limit of very low beta and sufficient density gradient. In an attempt to minimize electromagnetic effects on the momentum pinch, experiments were performed in MAST L-mode plasmas at relatively low beta (β_N=2, β_T=4%) (no perturbative data is available from NSTX L-modes). The discharges under investigation are lower-single-null (LSN) diverted L-mode plasmas with a toroidal magnetic field B_T=0.5 T, plasma current of I_p=400 kA ($q_{95}\approx 5.3$, R/a=0.88/0.55 m), line-averaged density $\langle n_e\rangle\approx 2.3\times10^{19}$ m^{-3} and NBI heating power P_{NBI}=2 MW using one co-I_p directed beam injector. The plasmas exhibit sawteeth, which will be discussed further below. Following the approach taken in the NSTX H-mode experiments [6], short n=3 magnetic perturbations (20 ms ramp-up, 40 ms flattop, 20 ms ramp-down) were applied to briefly perturb the plasma rotation via neoclassical toroidal viscosity (NTV), so that the transient response can be used to infer χ_φ and V_φ.

Time-traces of relevant parameters for three 400 kA L-modes are shown in Fig. 3 including I_p, P_{NBI}, line-integrated density (n_eL), stored energy, β_N, lower-divertor D_α, and n=3 coil current. Shots 29890 and 29892 are repeat shots that have three n=3 pulses, while shot 29891 is a reference shot with no applied n=3 field. During the plasma current flat-top, after t>300 ms the density reaches a stationary state. With the application of n=3 fields (t=0.33-0.41 s) there is a small but noticeable density pump out ($\Delta n/n{\sim}5\%$), as observed previously in MAST L-mode using even parity n=3 perturbations [16]. There is a corresponding ~15-20% drop in stored energy and beta. In the baseline discharge without n=3 fields an L-H mode transition eventually occurs at t=470 ms. This is consistent with the previously observed delay or suppression of L-H transition in MAST plasmas using n=1,2, and 3 field perturbations [17]. The analysis in the remainder of the paper focuses on the time-window between t=0.3 – 0.45 s, which includes just before, during, and after the second n=3 field pulse when all three discharges remain in L-mode.

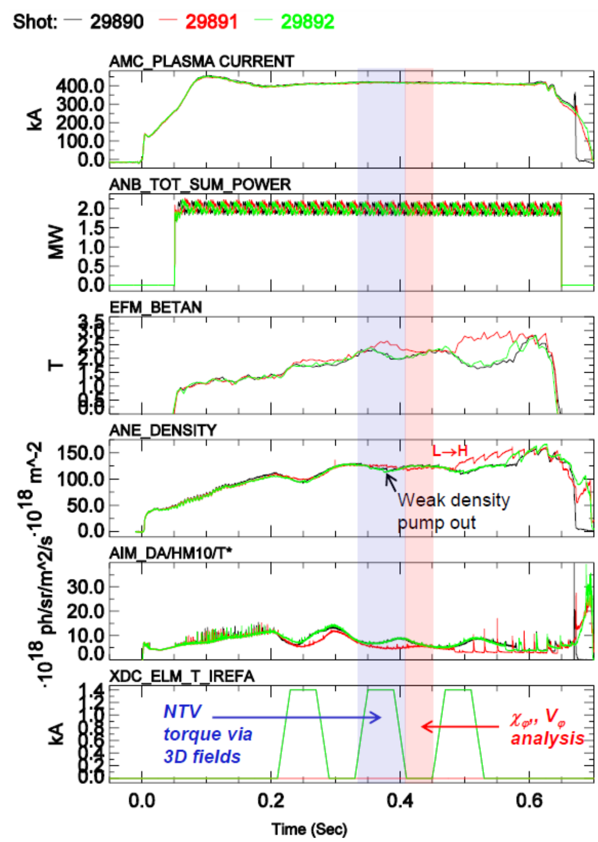

Fig. 3. Time traces of plasma current, total injected beam power, normalized beta, line-averaged density, divertor D-alpha, and applied n=3 current for three MAST L-mode discharges. The region shaded in red is used for the perturbative momentum transport analysis.

Fig. 4 shows the rotation evolution at a few spatial locations for the discharge with n=3 fields (29890, black) and without (29891, red), measured by a 64 channel charge exchange recombination spectroscopy system (CXRS) with ~1 cm and 5 ms spatial and time resolution, respectively [18]. The peak toroidal rotation rate is $\Omega\approx75$ krad/s, which corresponds to $V_{tor}\approx75$ km/s or a Mach number of $Ma=v_{Tor}/c_s=0.4$ (using $c_s=(T_e/m_d)^{1/2}$), and falls off to ≤5 krad/s towards the plasma edge. The dashed line shows the raw CXRS data, where the small oscillations associated with the sawteeth are apparent. The sawteeth have an average period of 12 ms, so to help clarify the slower response of the rotation to the applied n=3 field, a 3-point (15 ms) moving-average boxcar filter is applied as shown by the solid lines.

While the rotation is not completely stationary leading up to the energizing of the n=3 field (t=0.33 s), there is a clear response compared to the case without n=3 fields. This response is seen across the entire minor radius from the edge in to the magnetic axis. The magnitude of the perturbed toroidal angular rotation $\Delta\Omega$ ranges between 3 krad/s at the edge to 20 krad/s near the axis. After the turn-off of the n=3 fields (t=0.41 s), the rotation recovers and approaches the value of rotation for the reference shot for almost all radii except those nearest the magnetic axis. The braking of rotation during the n=3 perturbed field is used to infer torque due to neoclassical toroidal viscosity (NTV). The response of the rotation after removal of the n=3 field, where precise knowledge of the NTV torque is unnecessary and the torque from NBI heating can be accurately calculated, is used to infer χ_φ and V_φ below.

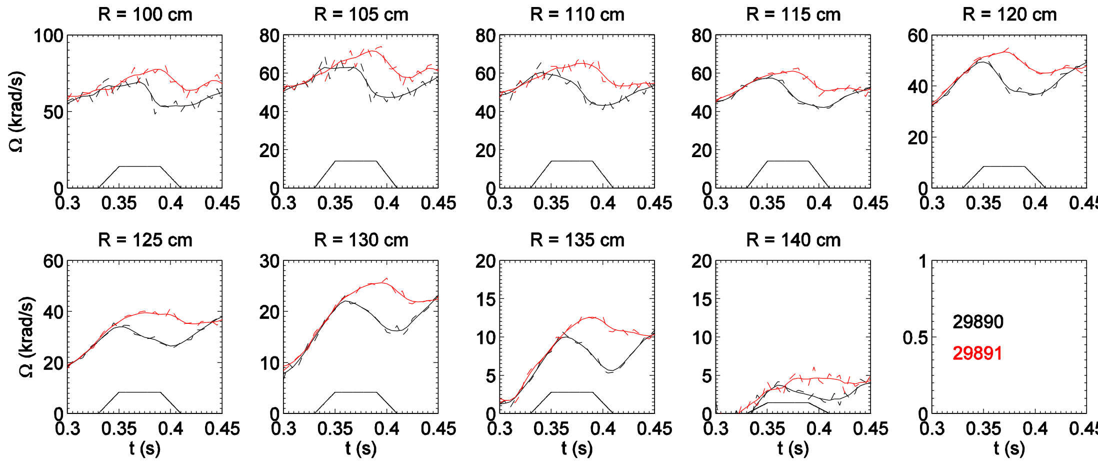

Fig. 4. Time history of toroidal rotation at multiple radii in two shots from Fig. 3. Dashed lines are the raw data, solid lines are the filtered signals.

Inspection of the Mirnov coils shows there is no persistent low-frequency MHD activity that could potential influence the rotation response, such as that from the so-called long-lived mode [19]. However, a change in rotation is observed around the sawteeth that are present. As the time-resolution of the CXRS measurement (5 ms) is far too slow to capture the fast transient response of the sawteeth, conditional averaging has been used to inspect how much the ensemble-averaged rotation changes using the two nearest measurements, before and after, each given sawtooth time. The same conditional averaging has been applied to the ion temperature measurements, as well as electron density and temperature from Thomson scattering (with a time resolution of 4.2 ms) [20].

Fig. 5 shows the results of the conditional averaging using 12-14 sawteeth in each discharge in the 15 ms time window t=0.3-0.45 s. The electron temperature near the magnetic axis (R=0.99 m) drops ΔT_e=-120 eV (16% of T_{e0}) after the sawtooth crash, and there is a modest increase +50 eV 15-20 cm away from the axis. The ion temperature shows a similar response with a -60 eV drop (6% of T_{i0}) at the axis and +20 eV increase 15-20 cm away. The inversion radius of ΔT_e and ΔT_i corresponds with the radius where the q=1 surface from MSE-constrained EFIT++ reconstructions is predicted to occur ($R_{out,q=1}$=114-118 cm), as indicated by the vertical blue dashed lines.

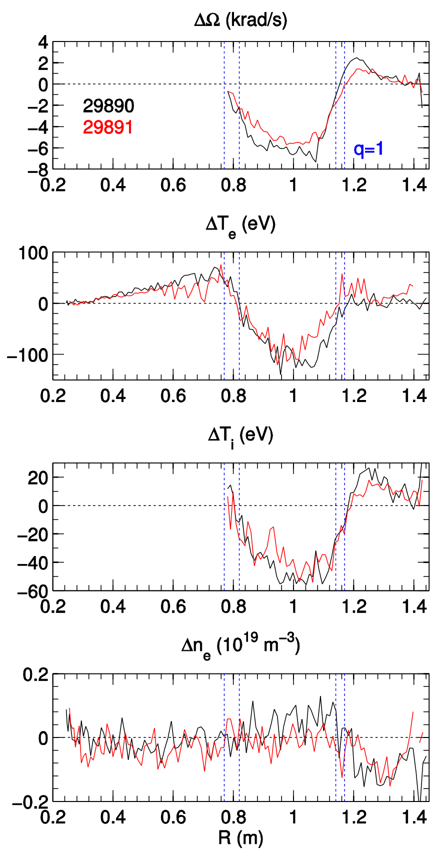

Fig. 5. Average change in rotation, temperature and electron density conditionally averaged for time-slices before and after sawteeth.

The average period of sawteeth (Δt_{ST}=12 ms) is shorter than the time intervals to be used for perturbative momentum transport analysis (≥30 ms). Furthermore, as we will see below the transport analysis is most useful outside the inversion radius where the amplitude of rotation change is much smaller than that due to the applied n=3 fields. We therefore assume that the momentum transport analysis is valid using the time-filtered signal that eliminates the sawteeth effects on the rotation (as shown in Fig. 4).

The flux-surface averaged, 1-D toroidal angular momentum equation solved by TRANSP [21] is [22,23]:

$$\frac{\partial}{\partial t}\left(\sum_i n_i m_i \langle R^2\rangle \Omega\right)+\frac{1}{V'}\frac{\partial}{\partial \rho}\left[V'\cdot\Pi\right]=T_{NBI}-T_{sink}$$

using the radial coordinate $\rho=(\Phi/\Phi_{LCFS})^{1/2}$, where Φ is the toroidal flux, $V'=dV/d\rho$, T_{NBI} represents the torque source from NBI deposition (J×B and collisional) calculated from NUBEAM [24], and T_{sink} represents all the torque sinks including charge-exchange losses, ionization losses, and NTV torque when the n=3 coils are energized.

The perturbative momentum transport analysis is applied during a 30 ms time window after the n=3 fields are removed so that we can assume T_{NTV}=0. Assuming the momentum flux has only diffusive and convective components, $\Pi_\varphi = n_i m_i \langle R^2\rangle(-\chi_\varphi \nabla\Omega + V_\varphi \Omega)$, where Π_φ is determined from TRANSP at 60 radial grid zones, we solve for χ_φ and V_φ using the measured response of $\Omega(t)$ and $\nabla\Omega(t)$.

The solid data points in Fig. 6 show the resulting fit of χ_φ and V_φ, assuming they are constant in time. In this region the perturbative analysis indicates an inward directed momentum pinch with velocities between V_φ= -5 ms to -30 ms. The value of the inferred pinch is comparable to that found in NSTX H-modes. The corresponding momentum diffusivity χ_φ=2-4 m^2/s is similar to the ion thermal diffusivity in this region, and is larger than the effective momentum diffusivity, $\chi_{\varphi,eff}$~1.8 m^2/s determined from TRANSP (i.e. the purely diffusive case, V_φ=0, red in Fig. 6).

In the middle of the analysis region (ρ~0.6) the correlation between $\Omega(t)$ and $\nabla\Omega(t)$ is very strong (Pearson product R>0.9) such that the solutions for χ_φ and V_φ become non-unique. As a result, the fit tends towards very large values of χ_φ and V_φ in this location (data points not shown). However, there is no particularly strong variation in plasma profiles in this region, so we further assume that the transport coefficients should vary smoothly in radius. Therefore, instead of fitting the transport relationship for each radii independently, a parameterized form for the transport coefficients can be used to solve for the χ_φ and V_φ profiles constrained using the entire analysis region (ρ=0.5-0.7) simultaneously. This allows for a unique solution of $\chi_\varphi(\rho)$ and $V_\varphi(\rho)$ profiles even in the region where there is strong correlation between $\Omega(t)$ and $\nabla\Omega(t)$. Polynomial expansions up to 7th order were tried, with a best fit occurring using 2nd order. The resulting fit profiles of transport coefficients smoothly connect the values found in the single-radius fit procedure, as shown by the solid black lines in Fig. 6. The fit also give a smaller reduced χ_ν^2 compared to the local fits.

As shown in Fig. 3, there is a ~15-20% reduction and recovery in stored energy during and after the applied 3D field perturbations. A similar variation is seen in the TRANSP ion and electron thermal diffusivities, so it is natural to assume that the momentum transport coefficients might also follow this same trend. If the above fitting procedure is applied assuming time-dependent $\chi_\varphi(t)$, $V_\varphi(t)$ that follow the ~20% variation in thermal diffusivities, smaller magnitudes of $\chi_\varphi(r)$ and $V_\varphi(r)$ are inferred, given by the dashed lines in Fig. 6. While the reduction in diffusivity is roughly a factor of two, the momentum pinch

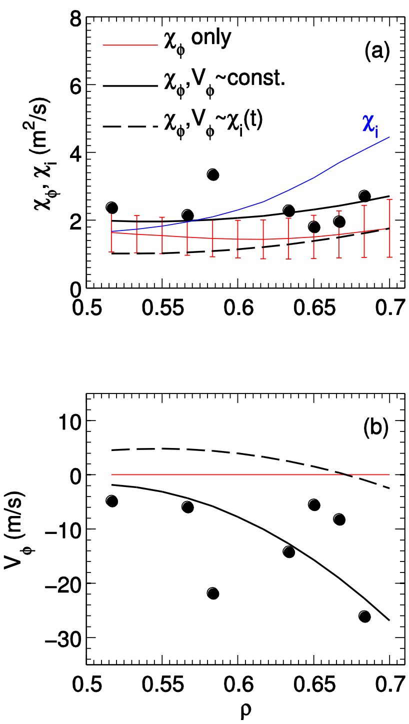

Fig. 6. (a) Profiles of fit χ_φ assuming only diffusive transport (red) or diffusive and convective transport (black). The symbols are from the direct fit at each radii, while the lines assume a polynomial radial dependence that is constant in time (solid black) or time-dependent proportional to $\chi_i(t)$ (dashed black). Also shown is the time-averaged total ion thermal diffusivity (solid blue). (b) The corresponding profiles of the fit momentum convection coefficient, V_φ.

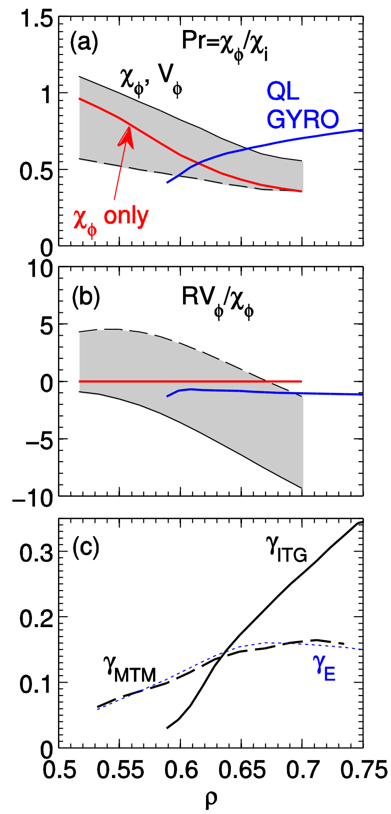

Fig. 7. (a) Prandtl number χ_φ/χ_i from the various fits described in Fig. 6. (b) Corresponding pinch parameter RV_φ/χ_φ. The blue lines show the predicted Pr and RV_φ/χ_φ from local, quasi-linear GYRO simulations of the ITG instability (evaluated at $k_\theta\rho_s$=0.4). (c) Linear growth rates of ITG and MTM instabilities (black), and E×B shearing rate (blue).

is reduced significantly (in magnitude) to the point that it is near zero or outward directed over most of the analysis region. This adds considerable uncertainty in inferring the presence of a momentum pinch. We note that no significant variation in energy confinement was observed in the NSTX H-mode experiments utilizing the 3D field perturbations, so this particular source of uncertainty did not appear in those discharges.

The Prandtl number (Pr=χ_φ/χ_i) and pinch parameter derived from the fit coefficients above are shown in Fig. 7 for both time-independent (solid black line) and time-dependent (dashed black line) fits. The grey shaded region spans the two fits and provides a worst-case uncertainty estimate. The range of Pr≈0.5-1.1 from the (χ_φ,V_φ)~constant fits is similar to many previous tokamak results, and is a bit smaller Pr≈0.3-0.6 for the (χ_φ,V_φ)~χ_i(t) fit. The pinch parameter is between RV_φ/χ_φ=(-1)-(-9) for the (χ_φ,V_φ)~constant fit, similar to the NSTX H-mode values, but spans RV_φ/χ_φ=(-1)-(5) for the (χ_φ,V_φ)~χ_i(t) fit.

Linear GYRO simulations for this case predict that a broad spectra of electrostatic ITG modes are unstable outside ρ>0.6 as expected for an L-mode discharge. Fig. 7c shows the radial profile of growth rates near the most unstable wavenumber ($k_\theta\rho_s$=0.4). Somewhat surprising is that the electromagnetic MTM is also predicted to be unstable over the entire analysis region ρ=0.5-0.7, illustrating that beta is still sufficiently large in these lower power ST L-modes to drive electromagnetic microinstabilities. However, the E×B shearing rates (γ_E) are as large as the MTM growth rates suggesting these modes should be supressed nonlinearly, whereas γ_{ITG} > γ_E outside ρ>0.62, implying ITG turbulence can survive in this region of the plasma.

The Pr and RV_φ/χ_φ numbers computed from the ratio of quasi-linear fluxes for the ITG instability are shown in Fig. 7a,b. The Prandtl numbers fall within the range of experimentally inferred values, although they do not follow the same radial profile. The predicted pinch values are inward and are very small in magnitude, $(RV_\varphi/\chi_\varphi)_{ITG}$~(-1). These predictions are similar to the NSTX L-mode calculations discussed above, consistent with the normalized density gradients in this region being relatively small (R/L_{ne}<2.5). They also fall within the range of inferred momentum pinch, but the experimental uncertainties are too large to validate the accuracy of the predicted weak momentum pinch.

4. Summary and discussion

Quasilinear gyrokinetic predictions of momentum pinch in NSTX H-modes are unable to reproduce the inferred momentum pinch values from perturbative experiments. This is due to the influence of electromagnetic effects at high beta and low aspect ratio on the symmetry-breaking of the instabilities. To minimize electromagnetic effects, similar experiments were performed in lower beta MAST L-mode plasmas using 3D fields to perturb the plasma rotation. Assuming momentum transport coefficients that are constant in time gives similar pinch values to the NSTX H-mode cases, RV_φ/χ_φ=-1 to -9. However, if time-dependent coefficients are allowed to follow the ~15% deviations in thermal confinement due to the applied 3D fields (χ_φ,V_φ~χ_i(t)), the resulting pinch values are much smaller or even outward (RV_φ/χ_φ=-1 to 5). Quasilinear gyrokinetic simulations also predict a weak inward pinch in the L-mode case due to ITG instability, especially at finite beta and weak density gradient. Unfortunately the experimental uncertainties are too large to quantitatively validate the predictions. Future experiments are planned on NSTX-U to further probe the magnitude of momentum pinch and validate theory predictions at low aspect ratio using lower beta ST plasmas.

This research used resources of the National Energy Research Scientific Computing Center, supported by U.S. DOE Contract DE-AC02-05CH11231. This work is supported by US DOE contract DE-AC02-09CH11466 and the RCUK Energy Programme and EURATOM.

References

[1] M. Yoshida et al., Nucl. Fusion **52**, 123005 (2012).

[2] K. Ida, J.E. Rice, Nucl. Fusion **54**, 045001 (2014).

[3] P.H. Diamond, Nucl. Fusion **53**, 104019 (2013).

[4] A.G. Peeters et al., Phys. Rev. Lett. **98**, 265003 (2007); Nucl. Fusion **51**, 094027 (2011).

[5] T. Tala et al., IAEA FEC ITR/P1-19, San Diego (2012); H. Weissen et al., Nucl. Fusion **52**, 114024 (2012).

[6] W. Solomon et al., Phys. Rev. Lett. **101**, 065004 (2008); S.M. Kaye et al., Nucl. Fusion **49**, 045010 (2009). W. Solomon et al., Phys. Plasmas **17**, 056018 (2010).

[7] W. Guttenfelder et al., Phys. Plasmas **23**, 052508 (2016).

[8] J. Candy and R.E. Waltz, Phys. Rev. Lett. **91**, 045001 (2003); J. Comput. Phys. **186**, 545 (2003).

[9] W. Guttenfelder et al., Nucl. Fusion **53**, 093022 (2013).

[10] E.A. Belli and J. Candy, Phys. Plasmas **17**, 112314 (2010).

[11] T. Hein et al., Phys. Plasmas **18**, 072503 (2011).

[12] Y. Ren et al., Nucl. Fusion **53**, 083007 (2013).

[13] A.G. Peeters et al., Phys. Plasmas **16**, 062311 (1009).

[14] R.L. Miller et al., Phys. Plasmas **5**, 973 (1998).

[15] G. Rewoldt, W.M. Tang, S. Kaye, J. Menard, Phys. Plasmas **3**, 1667 (1996).

[16] A. Kirk et al., Nucl. Fusion **50**, 034008 (2010).

[17] A. Kirk et al., Plasma Phys. **53**, 065011 (2011).

[18] N.J. Conway et al., Rev. Sci. Instrum. **77**, 10F131 (2006).

[19] M.-D. Hua et al., Plasma Phys. Control. Fusion **52**, 035009 (2010).

[20] R. Scannell et al., Rev. Sci. Instrum. **79**, 10E730 (2008).

[21] R.J. Hawryluk, Physics of Plasmas Close to Thermonuclear Conditions (Varenna, 1979).

[22] R.J. Goldston, Basic Physical Processes of Toroidal Fusion Plasmas (Varenna, 1985).

[23] J.D. Callen, A.J. Cole, C.C. Hegna, Nucl. Fusion **49**, 085021 (2009).

[24] A. Pankin et al., Comput. Phys. Commun **159**, 157 (2004).